# Fragmented Carbon Nanotube Macrofilms as Adhesive Conductors for Lithium-Ion Batteries

**Zeyuan Cao[†] and Bingqing Wei[†,‡,*]**

[†]Department of Mechanical Engineering, University of Delaware, Newark, Delaware 19716, United States and [‡]State Key Laboratory of Solidification Processing and School of Materials Science and Engineering, Northwestern Polytechnical University, Xi'an 710072, People's Republic of China

**ABSTRACT** Polymer binders such as poly(vinylidene fluoride) (PVDF) and conductive additives such as carbon black (CB) are indispensable components for manufacturing battery electrodes in addition to active materials. The concept of adhesive conductors employing fragmented carbon nanotube macrofilms (FCNTs) is demonstrated by constructing composite electrodes with a typical active material, $LiMn_2O_4$. The adhesive FCNT conductors provide not only a high electrical conductivity but also a strong adhesive force, functioning simultaneously as both the conductive additives and the binder materials for lithium-ion batteries. Such composite electrodes exhibit superior high-rate and retention capabilities compared to the electrodes using a conventional binder (PVDF) and a conductive additive (CB). An *in situ* tribology method combining wear track imaging and force measurement is employed to evaluate the adhesion strength of the adhesive FCNT conductors. The adhesive FCNT conductors exhibit higher adhesion strength than PVDF. It has further been confirmed that the adhesive FCNT conductor can be used in both cathodes and anodes and is proved to be a competent substitute for polymer binders to maintain mechanical integrity and at the same time to provide electrical connectivity of active materials in the composite electrodes. The organic-solvent-free electrode manufacturing offers a promising strategy for the battery industry.

**KEYWORDS:** adhesive conductor · conductive binder · lithium-ion batteries · carbon nanotube macrofilms · ultrasound

Active materials, conductive additives, and polymer binders are indispensable in conventional electrode design and manufacturing of lithium-ion batteries. Acetylene carbon black,[1,2] carbon nanotubes (CNTs),[3,4] and graphene[5,6] are the three most common conductive additives that construct a conductive matrix incorporating active materials spanning from positive materials, *e.g.*, $LiCoO_2$[7] and $LiFePO_4$,[8] to negative materials, *e.g.*, $Fe_2O_3$ and Si.[9,10] They not only provide superior electronic conductivities but also act as ideal mechanical supports to anchor and connect nanostructured active materials and sometimes as stress buffers to release the internal stress of the active materials resulting from the serious volumetric change and phase separation during insertion/extraction of Li ions. However, these conductive additives are barely used alone without any binder materials because it is commonly regarded that they cannot provide adhesive force for the active materials to withstand long charge/discharge cycles. Thus, it is necessary to turn to polymer binders such as poly(vinylidene difluoride) (PVDF),[11,12] phenol-formaldehyde (PF),[13] styrene butadiene rubber (SBR),[14] poly(acrylic acid) (PAA),[15] and carboxymethylcellulose (CMC)[16] to maintain mechanical integrity of the composite electrodes. Although the polymer binders play crucial roles in electrode manufacturing, their electrochemical inactivity contributes nothing but impairs the specific capacity of the entire electrode. To overcome these challenges, a strategy to employ conductive binders such as poly(9,9-diotylfluorene-*co*-fluorenone-*co*-methylbenzoic ester) (PFM),[18] polyaniline (PANi),[19] and poly(3,4-ethylenedioxythiophene) poly(styrenesulfonate) (PEDOT:PSS)[20] has been naturally proposed and extensively investigated to improve the capacity and lifetime of batteries. However, these conductive polymers typically cannot provide a comparable electronic conductivity to the carbon additives. They also inevitably involve expensive and toxic organic solvents such as *N*-methylpyrrolidone (NMP).[17] In parallel with this "bifunctional" concept, an adhesive conductor

* Address correspondence to (Bingqing Wei) weib@udel.edu.

Received for review January 28, 2014 and accepted February 24, 2014.

**Published online February 24, 2014**
10.1021/nn500585g

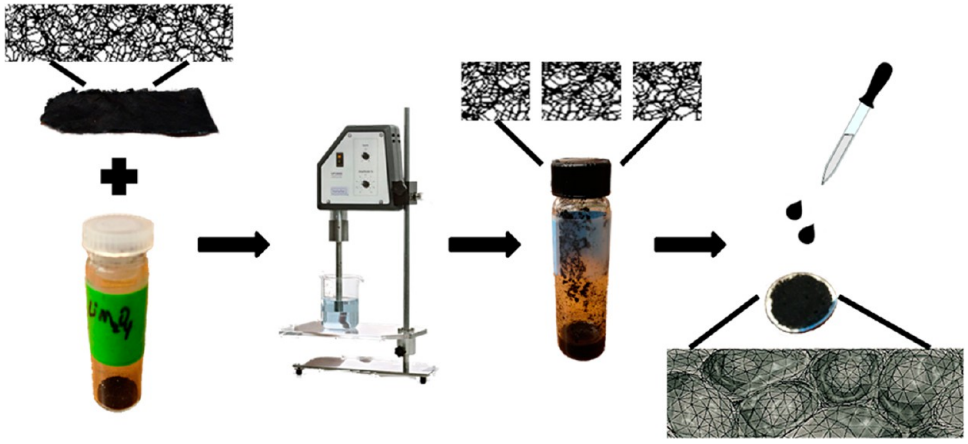

**Figure 1. Schematic illustration of the preparation of LMO−FCNT composite electrodes by ultrasound processing and drop casting.**

possessing both binding and conducting functions from pure carbon nanostructures is seldom reported. In fact, some specific forms of carbon such as stretchy uncrumbled graphene sheets do bear adhesive properties and could act as both conductive additives and binders.[21] Irregular, laterally 2-D distributed CNT segments are also proved to be able to enhance the adhesion force of vertically aligned CNT arrays, which could perform the mechanical binding function inspired by gecko feet.[22] Overall, these adhesive conductors can not only form pathways for facilitated transferring of lithium ions and electrons, improving battery performance, but also meet the desired goal of green chemistry, being friendly to the environment by avoiding the usage of NMP and other toxic organic solvents. Thus, in this article, we demonstrate the feasibility of the conceptual idea by applying fragmented CNT macrofilms (FCNT) as adhesive conductors in two demo-systems: two half-cells comprising positive material, $LiMn_2O_4$ (LMO), and negative materials, $Li_4Ti_5O_{12}$ (LTO), as working electrodes, respectively. Different from those nanoarchitectured carbon materials used as scaffolds such as CNT interconnected films,[23] 3-D CNT films,[24] and aligned-CNT films[25] with multiwalled CNTs in order to the achieve the "binder-free" goal, FCNT is in fact composed of single-walled CNTs (SWNTs). A SWNT has fewer defects and a resutling superior electrical conductivity. Moreover, rather than the stacked buckypapers or superaligned structures of the above-mentioned CNT films, the FCNT meshes are more like the cross-links in polymers entangled together with an adhesive property. They possess a stronger adhesive strength and have better electrochemical performance than conventional PVDF. To the best of our knowledge, this is the first report on the FCNT as a potential substitute of polymer binders for lithium-ion batteries.

## RESULTS AND DISCUSSION

**LMO−FCNT Half-Cell.** *Fabrication and Structural Characterization of LMO−FCNT Composite Electrodes.* The direct synthesis of SWNT macrofilms is enabled by a modified floating chemical vapor deposition (CVD) method using the solid volatile mixture of ferrocene/sulfur powders (atomic ratio Fe:S = 10:1) as precursors. The spinel LMO nanoparticles are prepared by a low-temperature hydrothermal method without any annealing processing according to the work of Jaephil Cho *et al.*[26] All the experimental details can be found in the Methods section and the published papers.[26,27] The fabrication procedures of the LMO−FCNT composite electrodes can be completed within three steps, as illustrated by the schematic in Figure 1. Samples coupling LMO with varied mass ratios of SWNT macrofilms, wherein 5, 15, and 30 wt % at maximum are chosen, are simply sonicated in an aqueous solution environment to obtain the desired uniform concentrations for coating on the aluminum substrates by drop casting. The entangled SWNT macrofilms are fragmentated to thousands of small FCNT meshes under the strong impact generated by ultrasound with medium amplitudes. These FCNT meshes function as intermediate layers similar to the cross-links linking the polymer chains by connecting the LMO nanoparticles to the current collector. On the one hand, they can easily wrap the LMO nanoparticles primarily due to their flexbile mesh structures and large surface areas. The functional groups such as carboxylic (−C−O) and hydroxylic (−O−H) groups on the surface of FCNT may enhance the tight anchoring of the LMO nanoparticles. On the other hand, the sticky edges of FCNT comprising the SWNT bundle tips, like the suckers of an octopus, hold hand in hand with the "tentacles" on the surface of the current collector, *i.e.*, the Al substrate, due to the rough contacts. The transmission electron microscopy (TEM) image of the as-prepared LMO nanoparticles in Figure 2a exhibits an agglomerate of cubic-shaped nanocrystals with a size in the range 10−50 nm. TEM images in Figure 2b and c reveal that the LMO nanoparticles are successfully anchored on the entangled SWNT bundles in the LMO−FCNT composites as expected. A high-resolution TEM (HRTEM) image (Figure 2d) clearly shows the fringe of lattice

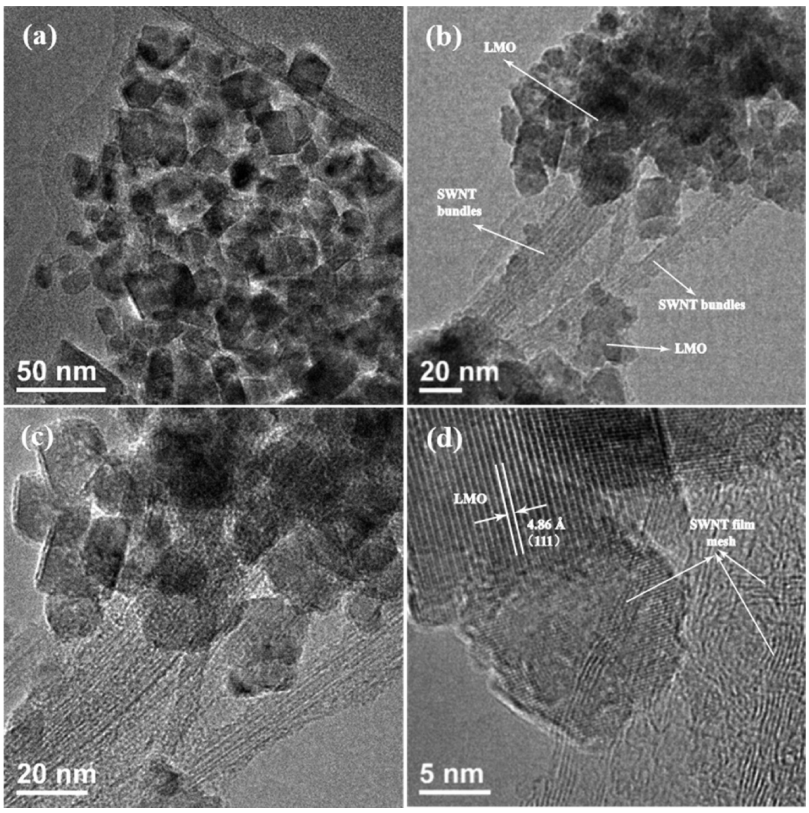


**Figure 2. (a) TEM and (b, c) high-magnification TEM images of LMO−FCNT and (d) HRTEM image of LMO−FCNT showing an individual LMO nanocrystal and the FCNT mesh.**

with a *d*-spacing of 4.86 Å assigned to the (111) planes of an individual LMO nanocrystal, through which the visibly "ripple"-like curved SWNTs in the interweaved FCNT meshes stretch. Indexing of the X-ray diffraction (XRD) patterns shown in the section Microstructure and Mechanical Characterization of LMO−FCNT Composite Electrodes, confirms the spinel structure of LMO with the *Fd*3*m* space group referenced to JCPDS 35-0782. The composition of the LMO−FCNT composite sample prepared with 30 wt % SWNT macrofilms but casted on the glass slide is examined by energy-dispersive X-ray spectroscopy (EDS) mapping. It shows that Mn element is homogeneously distributed in the carbon matrix, as shown in Supporting Information (SI) Figure S1a and b. The quantitative analysis of the EDS spectrum (SI, Figure S1c) shows that FCNT constitutes 27.5 wt % of the whole composite containing negligible amounts of impurities, Na, Si, Al, and S, which come from the glass slide substrate. The weight percentage of FCNT is in good agreement with the results of thermogravimetric analysis (TGA) in Figure S2 (SI), showing about 27 wt % FCNT. Note that the slight deviation (less than 3%) of mass loading from the initial input of 30 wt % justifies the desired uniform coupling of LMO with FCNT in compliance with the original weight ratios between LMO and the SWNT macrofilms.

*Electrochemical Characterization of LMO−FCNT Composite Electrodes.* The electrochemical performance of the LMO−CNT composite electrodes was evaluated in terms of specific capacity, rate capability, and cyclic stability by using the half-cells in the two-electrode configuration consisting of the LMO−FCNT composites and lithium metal as working electrodes and counter electrodes, respectively. The sample with 30 wt % FCNT is a representative to exemplify the electrochemical performance of the LMO−CNT composite electrodes. The charge and discharge curves with selected cycle numbers (1st, 2nd, 10th, 20th, 30th, 40th, and 50th) at the current density of 15 $mAg^{-1}$ exhibit a typical delithiation/lithiation behavior of LMO with two featured potential plateaus at around 4 and 4.15 V (Figure 3a). They are consistent with the two reversible redox couples, *i.e.*, 3.95 V/4.05 V and 4.1 V/4.2 V, which are indicative of the transformation between single cubic phases ($LiMn_2O_4 \leftrightarrow Li_{1-x}Mn_2O_4$) and the coexistence of two phases ($LiMn_2O_4$ and $Li_{0.2}Mn_2O_4$), respectively, as shown in the cyclic voltammetry (CV) plots (Figure 3b).[28] These two processes can be distinguished by the shape difference of the two redox couples, in that the former one at the lower potential is broader while the latter at the higher potential is sharper. It is also worth noting that the potential plateaus during discharge rise above the initial curve on cycling. Correspondingly, the anodic peaks in the CV curves shift to higher potentials. Figure 3c reveals that the capacity retention remains as high as 94% of

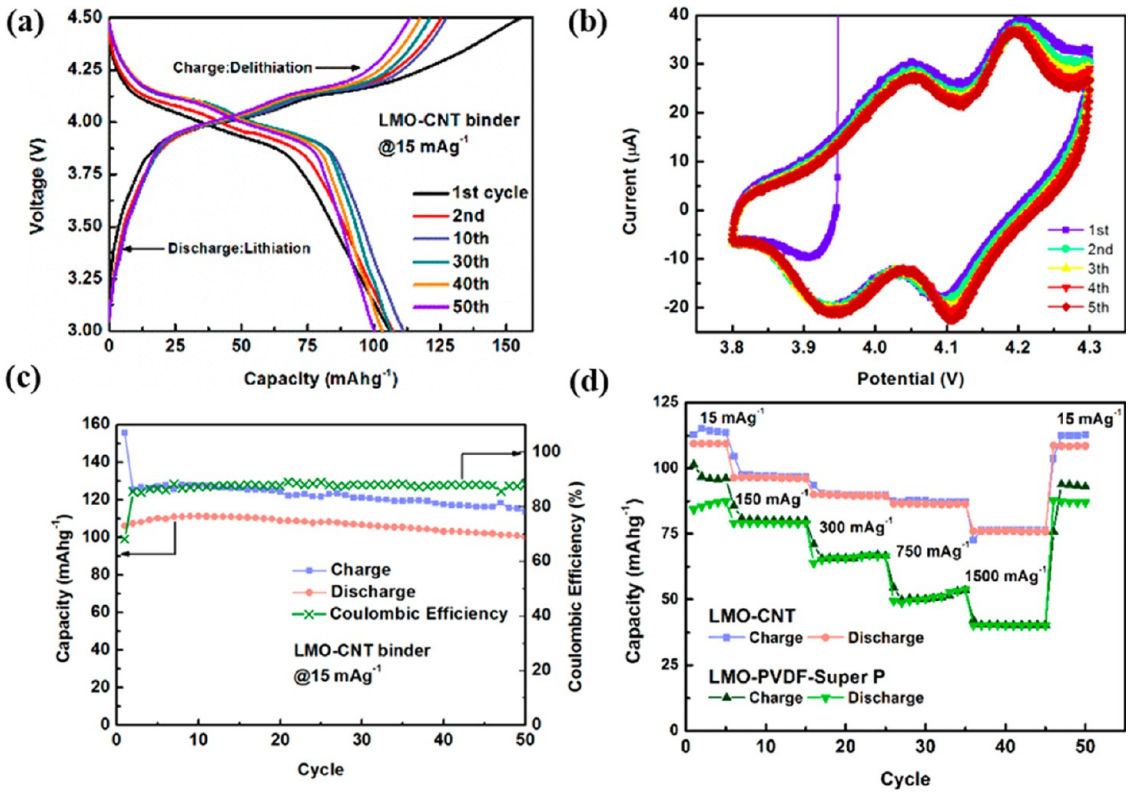


**Figure 3. (a) Galvanostatic charge/discharge voltage profiles of LMO−FCNT composite electrodes cycled at 15 mAg$^{-1}$. (b) CV curves of LMO−FCNT during the first five cycles. (c) Cycling performance of LMO−FCNT at 15 mAg$^{-1}$ for 50 cycles. (d) Comparison of rate capability between LMO−FCNT and LMO−PVDF−CB at different rates.**

the initial discharge charge capacity, *i.e.*, 106 mAhg$^{-1}$, after being charged and discharged for 50 cycles at the current density of 15 mAg$^{-1}$. Whereas, the average Coulombic efficiency (CE) is only 88%, departing farther from unity than that at faster rates shown in Figure 3d, where the high-rate capability of the LMO−FCNT composite electrodes has been demonstrated. The lower CE results from the cells cycled at lower rates having more time per cycle for parasitic reactions to occur and consume charges, such as electrolyte oxidation and loss of Li ions for solid electrolyte interface growth.[29] In contrast to the control electrodes with the same mass loading of LMO but 15 wt % of PVDF binders and 15 wt % of Super P carbon black instead (LMO−15 wt % PVDF−15 wt % CB, Figure 3d), LMO−FCNT overwhelms with higher capacities at all tested rates of 15, 150, 300, 750, and 1500 mAg$^{-1}$, and furthermore, the capacity difference becomes more evident as the rates increase. For example, the capacity comparison at the fifth cycle at the current density of 15 mAg$^{-1}$ is 109 mAhg$^{-1}$ *versus* 87 mAhg$^{-1}$ with a difference of 22 mAhg$^{-1}$, while it becomes 87 mAhg$^{-1}$ *versus* 49 mAhg$^{-1}$ at the 25th cycle when the current density increases to 750 mAg$^{-1}$ and, accordingly, the gap is enlarged to 38 mAhg$^{-1}$. The remarkable improvement in capacity definitely benefits from the substantially decreased resistance of charge transfer. This is indicated in the results of electrochemical impedance spectroscopy (EIS, detailed discussion as follows) by replacing the conventional PVDF and CB with the adhesive FCNT conductors, implying that the 2D FCNT mesh-bridged framework enables fast electronic and Li ionic transports. Subsequently, a cyclic stability measurement at a higher rate, 150 mAg$^{-1}$, for a longer time, 100 cycles, is conducted. The voltage profiles in Figure 4a show a similar behavior to that described above, where the potential plateau during discharge is increasing while the potential plateau upon charge is decreasing as the cycles proceed, which means a lower polarization and a higher efficiency. This is also in accord with the shift of the redox couple at 4.1 and 4.2 V to the opposite direction in the CV plots. The corresponding capacity retention in Figure 4b indicates a perfect performance with no deterioration, and the CE is approaching 100% since the 20th cycle, when it reaches equilibrium.

To study the effect of different contents of the adhesive FCNT conductors on the electrochemical performance of the LMO−FCNT composites, the galvanostatic charge−discharge (GCD) results at the current density of 150 mAg$^{-1}$ for 100 cycles for three samples with 5, 15, and 30 wt % of FCNT are presented in Figure 4c and d. From their GCD curves (Figure 4c), it can be seen that there is no difference except for the extending length of the potential plateau with increasing weight percentage of FCNT. Similar to each other in

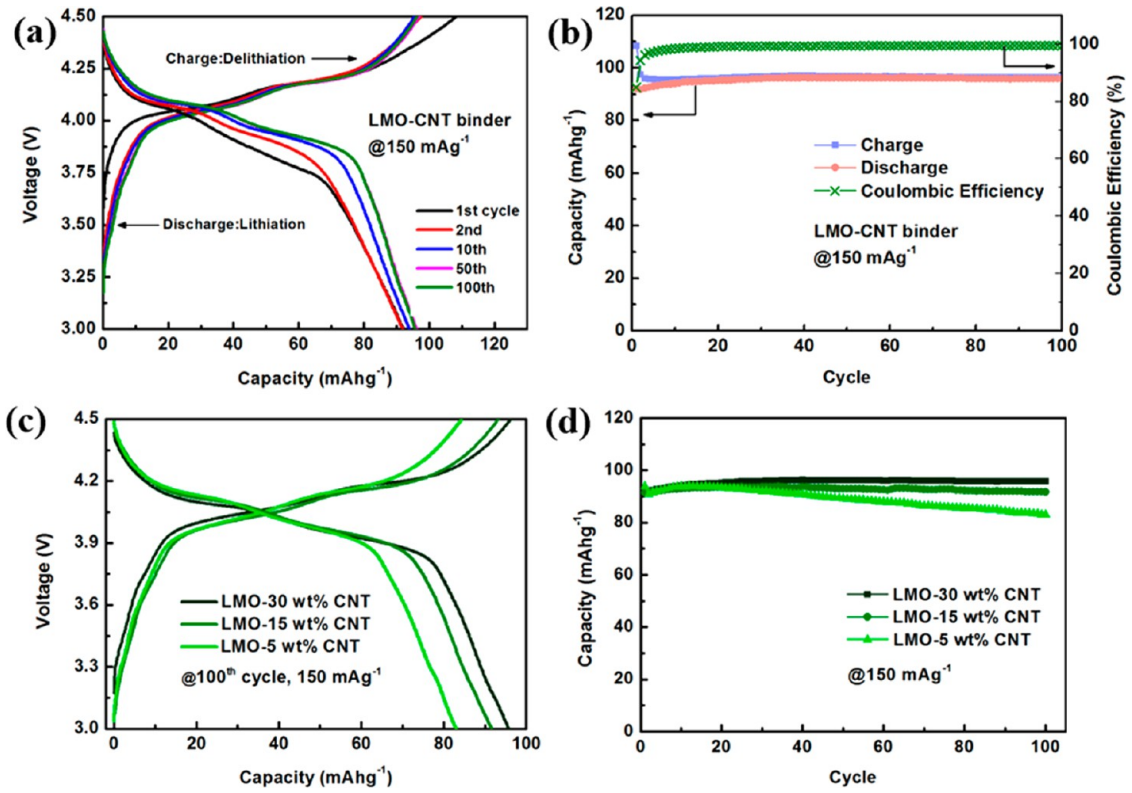


**Figure 4. (a) Galvanostatic charge/discharge voltage profiles of LMO−FCNT composite electrodes cycled at 150 mAg$^{-1}$. (b) Cycling performance of LMO−FCNT at 150 mAg$^{-1}$. Comparison of (c) voltage profiles for the 100th cycle and (d) cycling performance between LMO−30 wt % FCNT, LMO−15 wt % FCNT, and LMO−5 wt % FCNT at 150 mAg$^{-1}$.**

the trend of specific capacity retention as shown in Figure 4d, all three samples' capacities are increasing until the 20th cycle, at which point the samples with 5 and 15 wt % FCNT start fading while the LMO−30 wt % FCNT composite electrode remains stable. The capacity of LMO−5 wt % FCNT decreases faster with the decay slope of 0.15 mAhg$^{-1}$/cycle than LMO−15 wt % FCNT with 0.05 mAhg$^{-1}$/cycle. It can be inferred by linear interpolation that the decay slope would decrease to zero, which is equivalent to no capacity fading, when the weight of FCNT additives is increased to 20 wt % and above. This is experimentally confirmed with the 30 wt % FCNT sample. Thus, it is supposed that the electrochemical performance is determined by how much the resistance of charge transfer is decreased and how well the integrity of the composites is formed. EIS is used to support this reasoning. Figure 5a shows the Nyquist plots of four composite electrodes in fresh cells before cycling, including LMO−15 wt % PVDF−15 wt % CB, LMO−5 wt % FCNT, LMO−15 wt % FCNT, and LMO−30 wt % FCNT for comparison. A common Randles behavior is obviously observed for all the samples with a typical semicircle, of which the radius on the real axis is assigned to the resistance of charge transfer, in the midfrequency area.[30] Hence, without fitting curves by an equivalent circuit, it can be easily estimated that LMO−15 wt % PVDF−15 wt % CB has the largest charge-transfer resistance over 600 Ω, while the charge-transfer resistance of the LMO−FCNT composites has a decreasing trend from 250 Ω to 150 Ω and to 100 Ω as the FCNT content increases from 5 wt % to 15 wt % and then 30 wt %. The Bode phase plots (Figure 5b) could reveal information on the integrity of the composite electrodes. For the LMO−5 wt % FCNT sample, there is an evident separation of the two distinct peaks at 641 and 16681 Hz in the range of high frequency, which means the amount of FCNT is insufficient to integrally bind the LMO nanoparticles together. So is the curve for LMO−15 wt % PVDF−15 wt % CB, where a protruded shoulder at 148 Hz can be deconvoluted from the main peak at 5336 Hz. By contrast, LMO−15 wt % FCNT and LMO−30 wt % FCNT have good integrity because no phase separation appears in the Bode phase curves. Therefore, a combination of the best integrity with the best conductivity and the lowest charge-transfer resistance results in the best electrochemical performance of the LMO−30 wt % FCNT sample out of the four samples.

*Microstructure and Mechanical Characterization of LMO−FCNT Composite Electrodes.* To understand the correlation between the capacity retention of the LMO−FCNT composites and their microstructural evolution during GCD cycling, *ex situ* scanning electron microscopy (SEM) is implemented to compare the microstructures before and after the cycling measurements. In the left column of Figure 6, the images of a

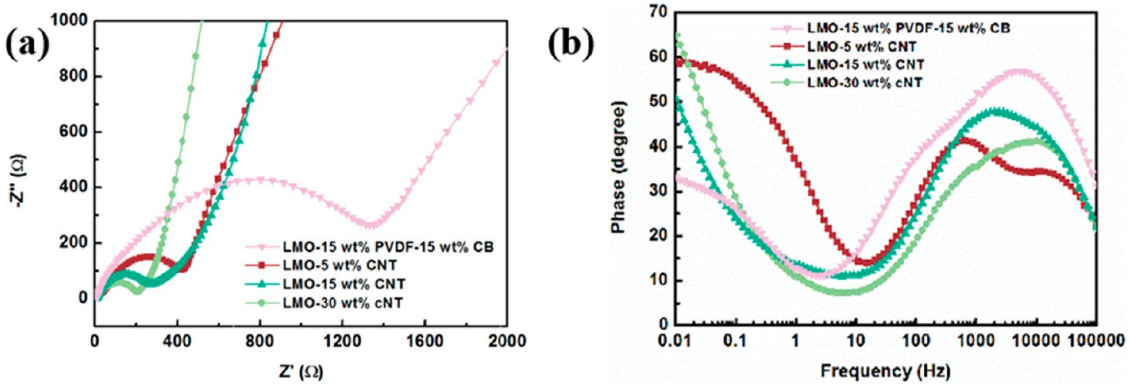


**Figure 5. Comparison of (a) Nyquist plot and (b) Bode phase plot between LMO–FCNT composites with different mass loadings of FCNT.**

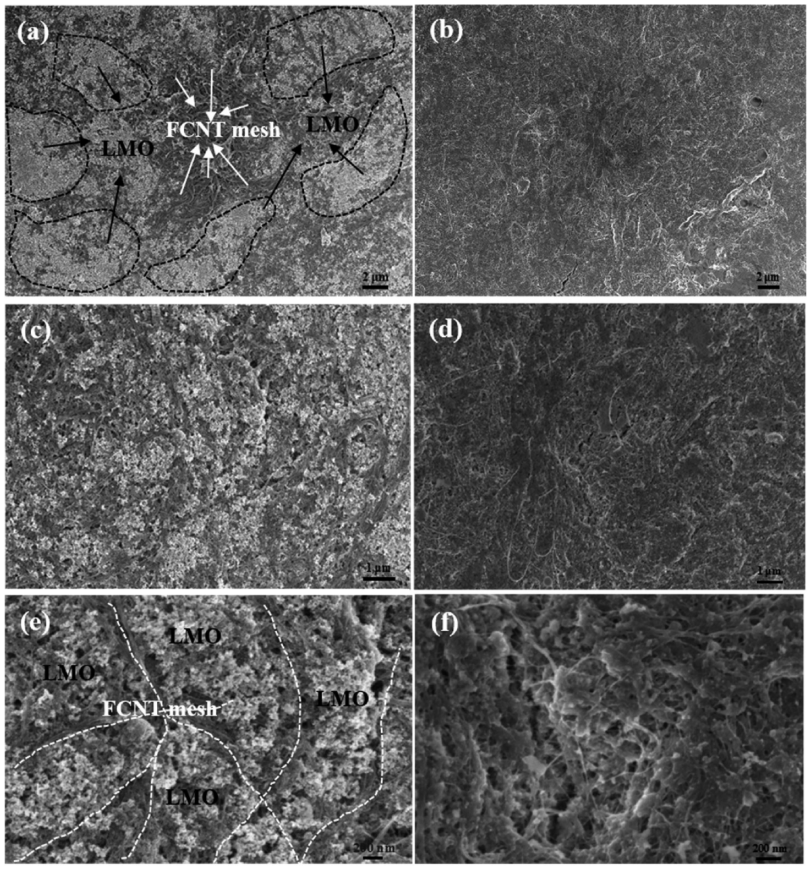


**Figure 6. SEM images of LMO–FCNT composite before (a, c, e) and after (b, d, f) cycling.**

fresh electrode in the sequence of increasing magnification from Figure 6a to c and e show the porous structures formed by the entanglement of the LMO–nanoparticle islands in the area of high brightness with the FCNT meshes in gray and dark parts. Basically, the LMO particles are uniformly distributed in the FCNT frameworks, which are enabled by an effective ultrasound treatment. After cycling for 100 cycles at 150 $mAhg^{-1}$, it is obviously seen that the pores are filled up through the solid electrolyte interface (SEI) layer coatings or residual electrolytes around the particles and SWNTs from Figure 6b, d, and f in the right column. The condensed morphology and structure enable a firmer association between LMO and the SWNTs, effectively inhibiting the LMO nanoparticles from dissolving into the electrolyte. The corresponding *ex situ* XRD results in Figure 7a present similar patterns, where only the slightly decreasing intensity is detectable at the featured peaks assigned to LMO, indicating the tiny loss of LMO nanoparticles after cycling. In addition, it is believed that the functional groups on the SWNTs may help enhance the binding of LMO with FCNT meshes. Figure 7b is the Fourier-transformed infrared (FTIR) spectrum of the LMO–FCNT composite

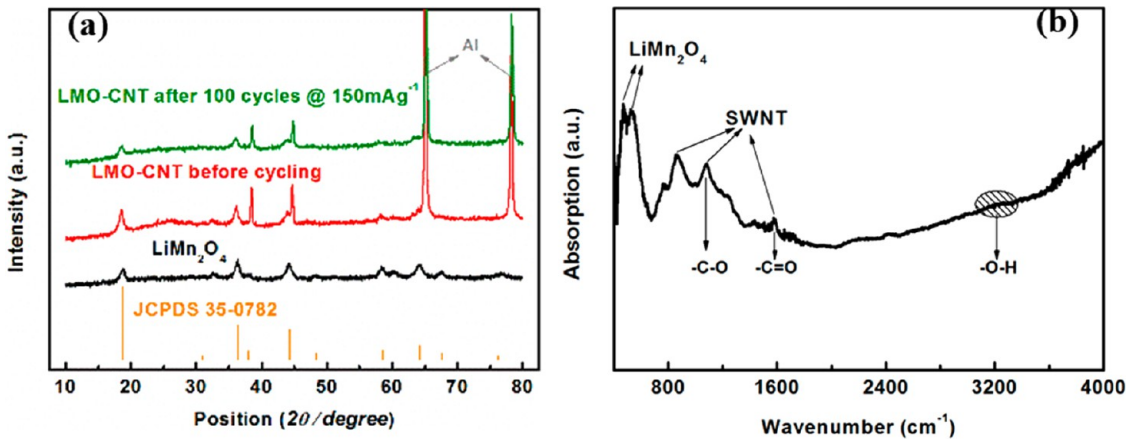


**Figure 7. (a) XRD patterns of pure LMO nanoparticles and LMO−FCNT composite before and after cycling. (b) FTIR spectrum of LMO−FCNT composite.**

electrode disassembled after cycling. The two absorption peaks below 600 $cm^{-1}$ are ascribed to the Mn−O vibrating modes of LMO.[31] The two peaks at 1100 and 1600 $cm^{-1}$ derive from −C−O stretching and conjugation of −C═O with C═C of the SWNT, respectively.[32] A broad peak with a weak intensity in the range 3100−3300 $cm^{-1}$ is assigned to −O−H stretching on the surface of the SWNT.[32] Thus, taking all the factors discussed above into account, the cyclic stability of the LMO−FCNT composite primarily benefits from the solid integral structures of LMO−FCNT.

The adhesion strength of the samples on current collectors, *i.e.*, the most relevant mechanical property for binders and adhesive conductors, is quantitatively evaluated by an *in situ* tribology method combining wear track imaging and force measurement. The working mechanism of this method is illustrated in the schematic in Figure S3 (SI). A hemisphere probe with a radius of 3.174 mm exerts a preload of 2500 mN on the samples and starts sliding at a speed of 25 $\mu$m/s on the sample films. The normal force $F_N$ and shear force $F_f$ are tracked in a time-series chart; meanwhile the morphology of the probe contact area is observed and imaged by an optical microscopy accessory. During the whole wear track, shear force $F_f$ increases quickly to reach a steady state and staying for a long time until declining. The adhesion strength $\sigma_A$ can be estimated by the equation $\sigma_A = F_f/A_c$, where $F_f$ is the critical shear force and $A_c$ is the contact area equal to 0.13 $mm^2$ by the Hertzian model.[33] The value of $\sigma_A$ is delimited within a range whose lower and upper limits are determined by two critical $F_f$ values corresponding to the occurrence of a large-scale failure and the steady state that a large area of substrate underneath is exposed to, as shown in Figure 8. The wear track images of LMO−30 wt % PVDF (Figure 8a) show not only an adhesive failure at the interface between the sample film and current collector but also a cohesive failure generated inside the sample film by the $F_f$ beyond the shear strength of the PVDF binders. In Figure 8b, only an adhesive failure for LMO−30 wt % FCNT occurs because SWNTs can hardly be separated because of their entangled feature and extremely high tensile strength, over 10 GPa, far exceeding the 50−57 MPa for PVDF.[34] It is also found that the failure area of LMO−30 wt % FCNT becomes disconnected after cycling, as shown in Figure 8c, which seemingly implies a weakened destruction, and the failure may be retarded. However, the directional coherence of the scratches indicates a cohesive failure. In fact, due to the brittleness of the SEI layer, the adhesion strength is therefore decreased from 7−10 MPa to 3.05−6.5 MPa after cycling. By comparing the electrochemical performance of the LMO−FCNT composites with different weight percentages of FCNT as well as their charge-transfer resistances discussed above, it is anticipated that the adhesive strength also positively correlates with the FCNT mass. This is confirmed in Figure 8d and e, where the large-scale failures occur immediately without a period of transition through a threshold of failure for both LMO−5 wt % FCNT and LMO−15 wt % FCNT samples. The mean values of the adhesive strength for the three LMO−FCNT samples along with LMO−30 wt % PVDF are summarized in the histogram (Figure 8f), where the upper limit and the lower limit of the adhesive strength for each sample are taken as the error limits denoted. The average adhesive strength of LMO−FCNT decreases from the maximum value of 8.5 MPa to 2.36 MPa and to a minimum, 1.07 MPa, as the FCNT amount decreases from 30 wt % to 15 wt % and then to 5 wt %. The 8.5 MPa for LMO−30 wt % FCNT also surpasses 7.15 MPa for LMO−30 wt % PVDF, justifying FCNT as a promising adhesive conductor that is never inferior to conventional binders. Such a high adhesion strength of FCNT is mainly attributed to the mechanical interlocking of the nanotubes at the asperities on the current collectors.[22]

**LTO−FCNT Half-Cell.** *Fabrication and Structural Characterization of LTO−FCNT Composite Electrodes.* To verify the general roles of FCNT as an adhesive conductor in

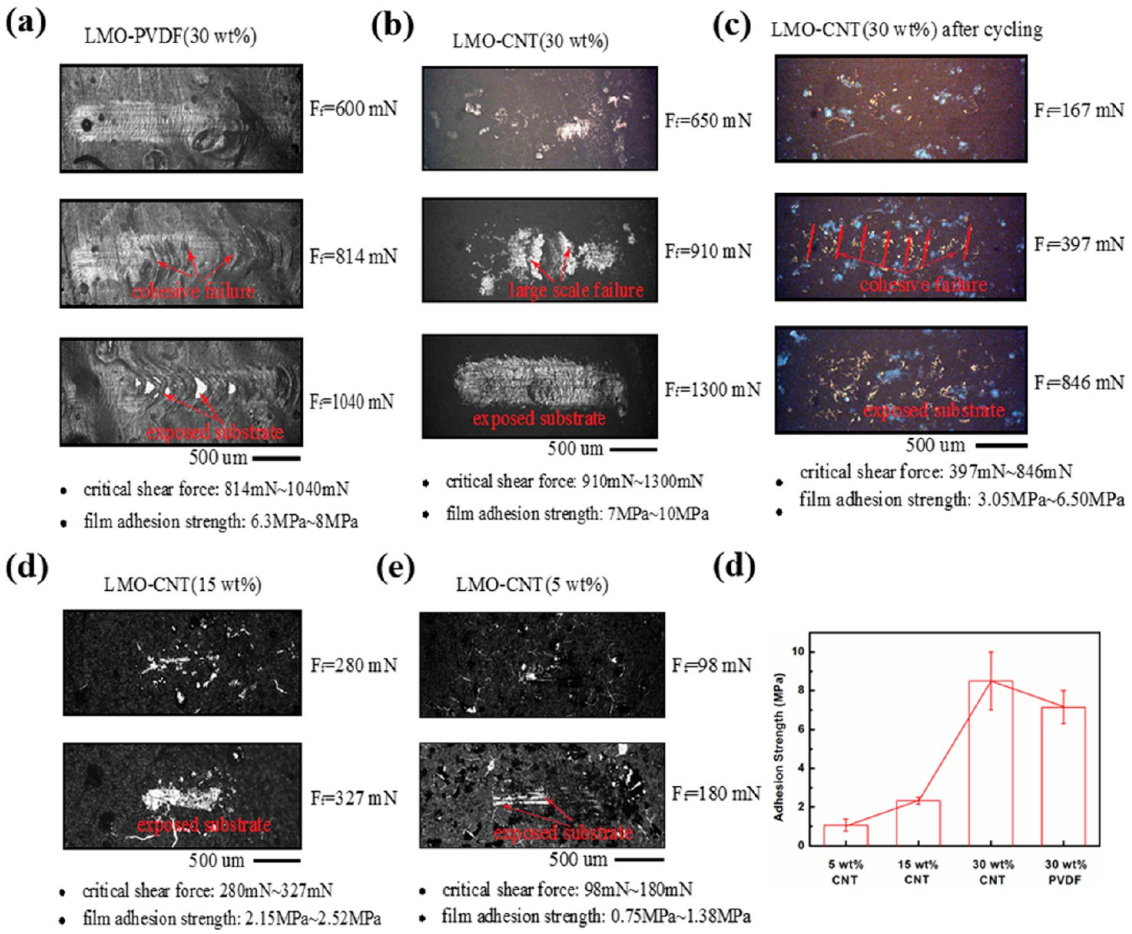


**Figure 8. Wear track images and adhesion strength of (a) LMO−30 wt % PVDF, (b) LMO−30 wt % FCNT before cycling, (c) LMO−30 wt % FCNT after cycling, (d) LMO−15 wt % FCNT before cycling, and (e) LMO−5 wt % FCNT before cycling. (f) Histogram of mean adhesion strength between LMO−30 wt % PVDF and LMO−FCNT with different mass loadings of FCNT.**

lithium-ion batteries, we extend the use of FCNT with anode materials. Herein our case is LTO, which has a theoretical specific capacity of 175 $mAhg^{-1}$ (denoted as 1 C).[35] This compatible capacity with that of LMO (~150 $mAhg^{-1}$) is important for pairing them to construct a full cell with two electrodes in balanced weight. The synthesis of LTO is also carried out by a low-temperature hydrothermal method similar to that of the spinel LMO nanocrystals in Section 2.1.1. The electrode preparation is also the same except using Cu instead of Al as the current collectors. All details can be found in the Methods section. The morphology of the LTO−FCNT composite is similar to that of LMO−FCNT, as shown in Figure 9a and b. The SEM images present a porous structure framed by FCNT meshes, in which LTO nanoparticles of large size or in aggregation are embeded, while those of smaller size are anchored on the SWNT bundles. Besides these similarities, it is worth noting that unlike the LMO prepartion method, where no heat treament is needed to obtain the final LMO products in spinel structure, annealing the precipitates collected from the hydrothermal reaction in Ar atmosphere at 500 °C for 5 h is an indispensible step for phase transition from an intermediate product of Li-intercalated rock-salt-type $LiTiO_2$ to spinel $Li_4Ti_5O_{12}$. This is proved by indexing the XRD data (Figure 9c) according to JCPDS 49-0207 and JCPDS 16-0223.

*Electrochemical Characterization of LTO−FCNT Composite Electrodes.* The electrochemical behavior of the LTO−FCNT composite electrodes is investigated in half-cells with Li metal as counterelectrodes by a series of GCD measurements. In the voltage profiles (Figure 10a) for selected cycles at varied rates from 1 C to 20 C, the well-defined long and flat discharge and charge potential plateaus at around 1.5 and 1.6 V *versus* $Li^+/Li$ indicate the reversible $Li^+$ insertion and extraction processes ($Li_4Ti_5O_{12} \leftrightarrow Li_7Ti_5O_{12}$).[35] The corresponding rate capabilities in Figure 10b show that the specific discharge capacity decays from an initial 182 $mAhg^{-1}$ to 125 $mAhg^{-1}$ at the end of the 10th cycle at 1 C rate and maintains 120 $mAhg^{-1}$ at 5 C for the following 10 cycles. As it continues from the 20th to the 30th cycle at 10 C, the capacity retains a steady state of 100 $mAhg^{-1}$ followed by no more capacity fading within the last 10 cycles. The CE is approaching 100% since the first cycle. The cyclic performance of LTO−FCNT is tested at 1 and 10 C, respectively for 200 cycles. By merging the GCD curves at 1 C (Figure 10c, bottom) and 10 C (Figure 10c, top), it clearly shows that

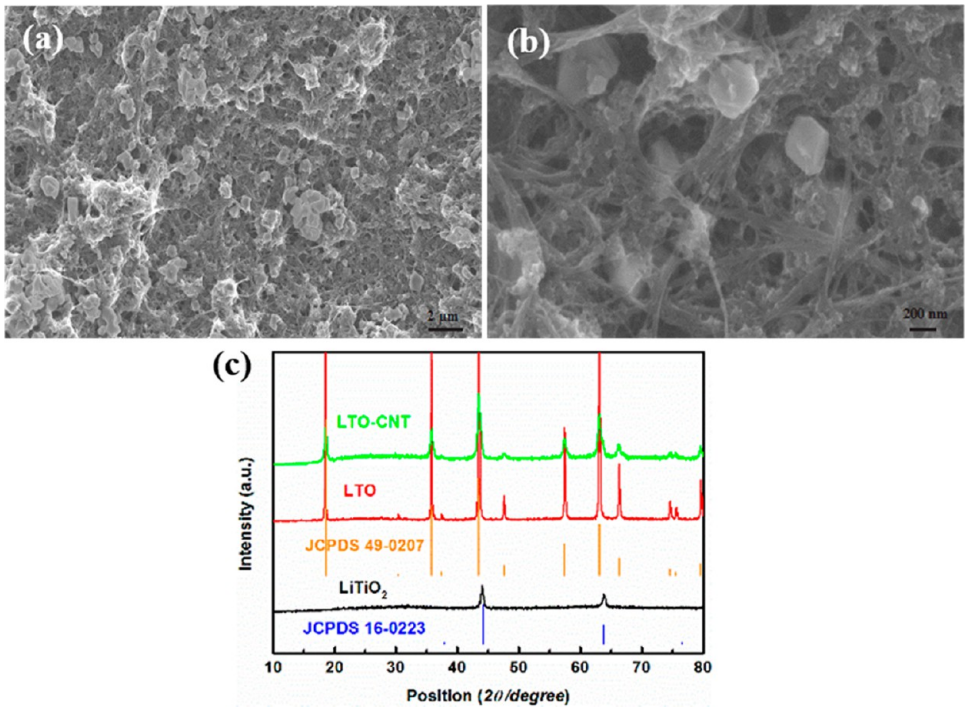


Figure 9. (a) SEM image and (b) high-magnification SEM image of LTO−FCNT composite. (c) XRD patterns of LTO nanoparticles before and after annealing in an Ar atmosphere and LTO−FCNT.

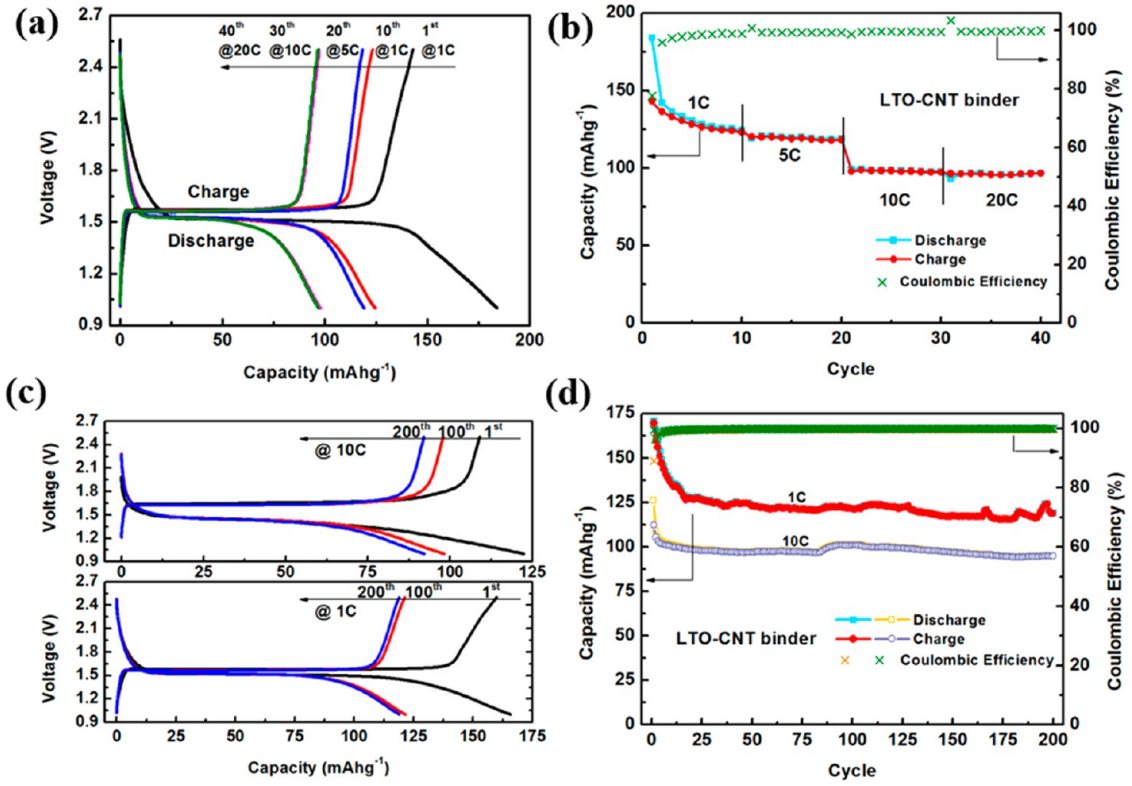


Figure 10. (a) Galvanostatic discharge/charge voltage profiles of LTO−FCNT composite electrodes cycled at different rates. (b) Rate capabilities of LTO−FCNT. Comparison of (c) galvanostatic discharge/charge voltage profiles and (d) cycling performance for LTO−FCNT cycled at 1 and 10 C.

the potential plateaus are not perfectly overlapped at first sight in Figure 10a. The discharge potential plateaus shift −0.1 V from 1.5 V to 1.4 V, while the charge plateaus shift +0.1 V from 1.6 V to 1.7 V. As a result, the polarization becomes evident with the enlarged potential gap between the two plateaus upon charge and

discharge by 0.2 V. This is the same case as LMO–FCNT described above. The capacity retention in Figure 10d agrees well with the rate capability. It shows a steady capacity of around 125 $mAhg^{-1}$ at 1 C after a substantial decrement in the first several cycles. At 10 C, the capacity remains at 100 $mAhg^{-1}$ since the third cycle, which has decreased from 125 $mAhg^{-1}$ at the first cycle. The CE also remains as high as 100%. Overall, the excellent electrochemical performance of the LTO–FCNT system proves the successful application of FCNTs as adhesive conductors for anodes in lithium-ion batteries.

## CONCLUSIONS

In summary, a concept of adhesive conductors is proposed with bifunctional roles as both conductive additives and binders for lithium-ion batteries. Fragmented carbon nanotube macrofilms are such adhesive conductors that can be coupled with active electrode materials to construct composite electrodes. They are assembled by a simple ultrasound processing and the drop-casting method. The electrochemical performance is exemplified by involving FCNT in the cathode material LMO and anode material LTO to form their respective half-cells with lithium metal. Compared with conventional PVDF binders, the adhesive FCNT conductors can significantly improve the rate capability and cyclic stability of LMO, which is due to their superior conductivity and solidly framed matrix in a porous structure, providing highly conductive pathways for electrons and fast transport channels for lithium ions. The tribology experimental results show that LMO–30 wt % FCNT has a higher adhesive strength than PVDF with the same mass loading. The successful uses of FCNT in both cathode and anode materials demonstrate that the adhesive conductor is an efficient strategy to substitute conventional binders in the battery industry.

## METHODS

**Synthesis of SWNT Macrofilms, $LiMn_2O_4$ and $Li_4Ti_5O_{12}$.** First, SWNT macrofilms were prepared using a modified floating chemical vapor deposition method according to previously published work.[27] In brief, the precursor, a mixture of ferrocene and sulfur (atomic ratio Fe:S = 1:10, both from Sigma Aldrich), was heated to 1100–1150 °C in a tube furnace with a mixed gas flow of Ar (1500 mL $min^{-1}$) and $H_2$ (150 mL $min^{-1}$). After 10–30 min reaction, the as-obtained unpurified SWNT macrofilms were transferred into a ceramic cubicle to be heat-treated at 450 °C in the air for 30 min. When the furnace was cooled to room temperature, the SWNT films were immersed in a concentrated HCl (37% by volume percent) solution for 72 h to remove the reddish $Fe_2O_3$ oxidized from Fe catalysts during the heat treatment. Then the films were rinsed with deionized (DI) water until the pH became neutral.

The $LiMn_2O_4$ nanoparticles were synthesized as Jaephil Cho *et al.* reported.[26] All the chemicals in the following were purchased from Sigma Aldrich and used as received. Solution A is prepared by dissolving 0.22 g of lithium hydroxide into 6 mL of DI water followed by adding 0.24 mL of hydrogen peroxide (30 wt %). A 0.69 g amount of manganese acetate dissolved in 6 mL of DI water forms solution B. Solutions A and B were blended with 20 mL of methanol and stirred for 20 min. Then the resulting blackish-brown slurry was transferred into a 40 mL Teflon-lined autoclave and hydrothermally reacted at 115 °C for 12 h. After the reaction was complete, the solid precipitates were collected and washed several times with DI water and ethanol. Finally, the black nanoparticles were dried in air at room temperature.

The $Li_4Ti_5O_{12}$ nanoparticles were synthesized by a similar method as follows. Briefly, 1.7 mL of hydrogen peroxide was dispersed in 0.4 M lithium hydroxide with 40 mL of methanol. Then 3 mM titanium(IV) butoxide was added to the above solution. After stirring for 1 h, the solution was poured into a 40 mL Teflon-lined autoclave, and the hydrothermal reaction was carried out at 130 °C for 12 h. Then the as-prepared white precipitates were washed *via* centrifugation with DI water and ethanol several times. After being dried completely in air overnight, the sample was annealed in Ar atmosphere at 500 °C for 5 h to obtain the final product, LTO nanoparticles.

**Preparation of LMO–FCNT and LTO–FCNT Composite Electrodes.** Freestanding SWNT macrofilms and LMO (LTO) nanoparticles are weighed by analytical microbalance (A&D Weighing). They were mixed in proper concentration with DI water followed by ultrasonication generated from ultrasonic power (UP200S, Hielscher Ultrasound Technology). The resulting ink solution consisting of CNT fragments coupling with LMO (LTO) nanoparticles was drop-casted on aluminum (copper) disks with a diameter of 1/2 in. as the current collectors. Then the electrodes were fabricated when the ink was dried. No organic solvents were employed. Three samples of LMO–FCNT composite electrodes with desired mass loadings of LMO were prepared: 5, 15, and 30 wt %. A sample of LTO (30 wt %) with FCNT was also prepared.

**Characterization.** The morphology and structure of the LMO–FCNT and LTO–FCNT were characterized by means of scanning electron microscopy (3 kV, Zeiss Auriga 60 FIB/SEM) and transmission electron microscopy (JEOL JEM-2010F). X-ray diffraction patterns were recorded within a $2\theta$ range of 10° to 80° at 0.02°/step and 2 s/step by a Philips X'Pert diffractometer with Cu Kα radiation. FTIR spectroscopy (Thermo-Nicolet Nexus 670) was operated from 4000 to 400 $cm^{-1}$. Thermogravimetric analysis was carried out on a high-resolution TGA instrument (Mettler-Toledo, SDA851e) from 0 to 1000 °C at a heating rate of 10 °C/min in flowing air.

**Electrochemical Measurements.** The mass of active materials was acquired by deducting the weight of bare Cu (Al) substrates from the whole weight of electrodes using a micro/ultramicro balance (Mettler Toledo XP6) with 0.001 mg accuracy. CR2032 coin cells were assembled in an argon-filled glovebox (MBraun UNIlab). Half-cells consist of the hybrid film as the working electrode, a Celgard 2500 as the separator, and a lithium ribbon (0.38 mm thick, 99.9%, Sigma Aldrich) as the counter electrode in 1 M $LiPF_6$ dissolved in 1:1 v/v ethylene carbonate/diethyl carbonate as electrolyte (Ferro Co.). The galvanostatic discharge–charge tests were carried out on BT-4 four-channel battery testing equipment (Arbin Instrument, Ltd.). Electrochemical impedance spectroscopy was performed on a PARSTAT 2273 potentiostat/galvanostat (Princeton Applied Research) with a 10 mV amplitude of ac signals from 100 kHz to 10 mHz.

*Conflict of Interest:* The authors declare no competing financial interest.

*Acknowledgment.* The authors thank J. X. Ye for conducting tribology measurements and helpful discussions. The authors gratefully acknowledge the financial support from the U.S. National Science Foundation (NSF) under contract no. CMMI-1067947. B.Q.W. acknowledges the Research Fund of the State Key Laboratory of Solidification Processing (NWPU), China (grant no. 83-TZ-2013).

*Supporting Information Available:* EDS mapping results, TGA curve, and *in situ* tribology illustration. This material is available free of charge *via* the Internet at http://pubs.acs.org.

## REFERENCES AND NOTES


1. Oh, S. M.; Oh, S. W.; Yoon, C. S.; Scrosati, B.; Amine, K.; Sun, Y. K. High-Performance Carbon-$LiMnPO_4$ Nanocomposite Cathode for Lithium Batteries. *Adv. Funct. Mater.* **2010**, *20*, 3260–3265.
2. Li, Y.; Tan, B.; Wu, Y. Mesoporous $Co_3O_4$ Nanowire Arrays for Lithium Ion Batteries with High Capacity and Rate Capability. *Nano Lett.* **2008**, *8*, 265–270.
3. Wang, W.; Kumta, P. N. Nanostructured Hybrid Silicon/Carbon Nanotube Heterostructures: Reversible High-Capacity Lithium-Ion Anodes. *ACS Nano* **2010**, *4*, 2233–2241.
4. Wen, Z.; Wang, Q.; Zhang, Q.; Li, J. *In Situ* Growth of Mesoporous $SnO_2$ on Multiwalled Carbon Nanotubes: A Novel Composite with Porous-Tube Structure as Anode for Lithium Batteries. *Adv. Funct. Mater.* **2007**, *17*, 2772–2778.
5. Paek, S.-M.; Yoo, E.; Honma, I. Enhanced Cyclic Performance and Lithium Storage Capacity of $SnO_2$/Graphene Nanoporous Electrodes with Three-Dimensionally Delaminated Flexible Structure. *Nano Lett.* **2008**, *9*, 72–75.
6. Wang, H.; Yang, Y.; Liang, Y.; Cui, L. F.; Sanchez Casalongue, H.; Li, Y.; Hong, G.; Cui, Y.; Dai, H. $LiMn_{1-x}Fe_xPO_4$ Nanorods Grown on Graphene Sheets for Ultrahigh-Rate-Performance Lithium Ion Batteries. *Angew. Chem.* **2011**, *123*, 7502–7506.
7. Antaya, M.; Dahn, J. R.; Preston, J. S.; Rossen, E.; Reimers, J. N. Preparation and Characterization of $LiCoO_2$ Thin Films by Laser Ablation Deposition. *J. Electrochem. Soc.* **1993**, *140*, 575–578.
8. Zaghib, K.; Shim, J.; Guerfi, A.; Charest, P.; Striebel, K. Effect of Carbon Source as Additives in $LiFePO_4$ as Positive Electrode for Lithium-Ion Batteries. *Electrochem. Solid-State Lett.* **2005**, *8*, A207–A210.
9. Cao, Z.; Wei, B. $\alpha$-$Fe_2O_3$/Single-Walled Carbon Nanotube Hybrid Films as High-Performance Anodes for Rechargeable Lithium-Ion Batteries. *J. Power Sources* **2013**, *241*, 330–340.
10. Yu, C.; Li, X.; Ma, T.; Rong, J.; Zhang, R.; Shaffer, J.; An, Y.; Liu, Q.; Wei, B.; Jiang, H. Silicon Thin Films as Anodes for High-Performance Lithium-Ion Batteries with Effective Stress Relaxation. *Adv. Energy Mater.* **2012**, *2*, 68–73.
11. Liu, G.; Zheng, H.; Simens, A.; Minor, A.; Song, X.; Battaglia, V. Optimization of Acetylene Black Conductive Additive and PVDF Composition for High-Power Rechargeable Lithium-Ion Cells. *J. Electrochem. Soc.* **2007**, *154*, A1129–A1134.
12. Maleki, H.; Deng, G.; Kerzhner-Haller, I.; Anani, A.; Howard, J. N. Thermal Stability Studies of Binder Materials in Anodes for Lithium-Ion Batteries. *J. Electrochem. Soc.* **2000**, *147*, 4470–4475.
13. Liu, G.; Xun, S.; Vukmirovic, N.; Song, X.; Olalde-Velasco, P.; Zheng, H.; Battaglia, V. S.; Wang, L.; Yang, W. Polymers with Tailored Electronic Structure for High Capacity Lithium Battery Electrodes. *Adv. Mater.* **2011**, *23*, 4679–4683.
14. Buqa, H.; Holzapfel, M.; Krumeich, F.; Veit, C.; Novak, P. Study of Styrene Butadiene Rubber and Sodium Methyl Cellulose as Binder for Negative Electrodes in Lithium-Ion Batteries. *J. Power Sources* **2006**, *161*, 617–622.
15. Li, J.; Le, D.-B.; Ferguson, P.; Dahn, J. Lithium Polyacrylate as a Binder for Tin-Cobalt-Carbon Negative Electrodes in Lithium-Ion Batteries. *Electrochim. Acta* **2010**, *55*, 2991–2995.
16. Kim, G.; Jeong, S.; Joost, M.; Rocca, E.; Winter, M.; Passerini, S.; Balducci, A. Use of Natural Binders and Ionic Liquid Electrolytes for Greener and Safer Lithium-Ion Batteries. *J. Power Sources* **2011**, *196*, 2187–2194.
17. Xun, S.; Song, X.; Battaglia, V.; Liu, G. Conductive Polymer Binder-Enabled Cycling of Pure Tin Nanoparticle Composite Anode Electrodes for a Lithium-Ion Battery. *J. Electrochem. Soc.* **2013**, *160*, A849–A855.
18. Zhang, H.; Cao, G.; Yang, Y. Carbon Nanotube Arrays and Their Composites for Electrochemical Capacitors and Lithium-Ion Batteries. *Energy Environ. Sci.* **2009**, *2*, 932–943.
19. Yu, G.; Hu, L.; Liu, N.; Wang, H.; Vosgueritchian, M.; Yang, Y.; Cui, Y.; Bao, Z. Enhancing the Supercapacitor Performance of Graphene/$MnO_2$ Nanostructured Electrodes by Conductive Wrapping. *Nano Lett.* **2011**, *11*, 4438–4442.
20. Lee, K.; Chromey, N.; Culik, R.; Barnes, J.; Schneider, P. Toxicity of *N*-Methyl-2-pyrrolidone (NMP): Teratogenic, Subchronic, and Two-Year Inhalation Studies. *Fundam. Appl. Toxicol.* **1987**, *9*, 222–235.
21. Luo, J.; Jang, H. D.; Huang, J. Effect of Sheet Morphology on the Scalability of Graphene-Based Ultracapacitors. *ACS Nano* **2013**, *7*, 1464–1471.
22. Hu, S.; Xia, Z.; Gao, X. Strong Adhesion and Friction Coupling in Hierarchical Carbon Nanotube Arrays for Dry Adhesive Applications. *ACS Appl. Mater. Interfaces* **2012**, *4*, 1972–1980.
23. Huang, J.-Q.; Peng, H.-J.; Liu, X.-Y.; Nie, J.; Cheng, X.-B.; Zhang, Q.; Wei, F. Flexible All-Carbon Interlinked Nano-architectures as Cathode Scaffolds for High-Rate Lithium-Sulfur Batteries. *J. Mater. Chem. A* **2014**, 10.1039/C4TA00245H.
24. Cheng, J.; Wang, B.; Xin, H. L.; Kim, C.; Nie, F.; Li, X.; Yang, G.; Huang, H. Conformal Coating of $TiO_2$ Nanorods on a 3-D CNT Scaffold by Using a CNT Film as a Nanoreactor: A Free-Standing and Binder-Free Li-Ion Anode. *J. Mater. Chem. A* **2014**, *2*, 2701–2707.
25. Wang, K.; Luo, S.; Wu, Y.; He, X.; Zhao, F.; Wang, J.; Jiang, K.; Fan, S. Super-Aligned Carbon Nanotube Films as Current Collectors for Lightweight and Flexible Lithium Ion Batteries. *Adv. Funct. Mater.* **2013**, *23*, 846–853.
26. Lee, S.; Cho, Y.; Song, H. K.; Lee, K. T.; Cho, J. Carbon-Coated Single-Crystal $LiMn_2O_4$ Nanoparticle Clusters as Cathode Material for High-Energy and High-Power Lithium-Ion Batteries. *Angew. Chem., Int. Ed.* **2012**, *51*, 8748–8752.
27. Zhu, H.; Wei, B. Direct Fabrication of Single-Walled Carbon Nanotube Macro-Films on Flexible Substrates. *Chem. Commun.* **2007**, 3042–3044.
28. Kim, D. K.; Muralidharan, P.; Lee, H.-W.; Ruffo, R.; Yang, Y.; Chan, C. K.; Peng, H.; Huggins, R. A.; Cui, Y. Spinel $LiMn_2O_4$ Nanorods as Lithium Ion Battery Cathodes. *Nano Lett.* **2008**, *8*, 3948–3952.
29. Smith, A.; Burns, J.; Dahn, J. A High Precision Study of the Coulombic Efficiency of Li-Ion Batteries. *Electrochem. Solid-State Lett.* **2010**, *13*, A177–A179.
30. Randles, J. Kinetics of Rapid Electrode Reactions. *Discuss. Faraday Soc.* **1947**, *1*, 11.
31. Chitra, S.; Kalyani, P.; Mohan, T.; Massot, M.; Ziolkiewicz, S.; Gangandharan, R.; Eddrief, M.; Julien, C. Physical Properties of $LiMn_2O_4$ Spinel Prepared at Moderate Temperature. *Ionics* **1998**, *4*, 8–15.
32. Kim, U. J.; Furtado, C. A.; Liu, X.; Chen, G.; Eklund, P. C. Raman and IR Spectroscopy of Chemically Processed Single-Walled Carbon Nanotubes. *J. Am. Chem. Soc.* **2005**, *127*, 15437–15445.
33. Schwarz, U. D. A Generalized Analytical Model for the Elastic Deformation of an Adhesive Contact between a Sphere and a Flat Surface. *J. Colloid Interface Sci.* **2003**, *261*, 99–106.
34. IDEMAT - Materials Selection Guide, http://www.idemat.nl/.
35. Feckl, J. M.; Fominykh, K.; Döblinger, M.; Fattakhova-Rohlfing, D.; Bein, T. Nanoscale Porous Framework of Lithium Titanate for Ultrafast Lithium Insertion. *Angew. Chem., Int. Ed.* **2012**, *51*, 7459–7463.